Sensorless control of IM for Limp-home mode EV applications

Ehsan Dehghan-Azad (corresponding author**), Shady M. Gadoue, and David J. Atkinson**

School of Electrical and Electronic Engineering, Newcastle University, Newcastle Upon-Tyne, NE1 7RU, UK. (email: e.dehghan-azad@newcastle.ac.uk; shady.gadoue@ncl.ac.uk; dave.atkinson@ncl.ac.uk)

Howard J. Slater, and Peter G. Barrass

Sevcon Ltd. Gateshead, NE11 0QA, UK. (email: howard.slater@sevcon.com; peter.barrass@sevcon.com)

Frede Blaabjerg

The Institute of Energy Technology, Aalborg University, Pontoppidanstraede 101, Aalborg, DK-9220, Denmark. (email: fbl@et.aau.dk)

Abstract

This paper presents a novel speed estimation scheme for induction motors (IMs) based on back electromotive-force model reference adaptive system (back-EMF MRAS). The scheme is employed for the purpose of sensorless fault tolerant Torque-Controlled Drives (TCD) used in a *limp-home* mode operation in electric vehicle (EV) applications. The proposed scheme was experimentally tested on a laboratory dynamometer using a 19 kW IM and a 29 kW controller, which both are currently used in the automotive industry for EV applications. The scheme was also implemented on an electric golf buggy which was equipped with a 5 kW IM. A performance comparison was carried out between the proposed and conventional back-EMF MRAS schemes for starting from standstill, sensitivity to parameter variations and constant speed operation with load variations. Utilizing the golf buggy, the behaviours of the new scheme was separately investigated for vehicle-starting from standstill, wide speed range including field weakening region and hill-starting operations. The proposed scheme is computationally easy to implement, robust against sensitivity to parameters variations, inverter non-linearity and errors due to digitization in the field weakening region. This scheme not only is consistent for vehicle-starting from standstill, it also provides a reliable vehicle-drive in the field weakening region and during vehicle hill-starting. The dynamometer

and vehicle test-drive results show the suitability of the proposed scheme for the purpose of EV fault tolerant *limp-home* mode operation.

Index Terms- Electric Vehicles (EVs), fault tolerant, Induction Motor (IM), Model Reference Adaptive System (MRAS), sensorless, Torque Controlled-Drive (TCD).

I. Introduction

In recent years, the electrification concept in the automotive industry has gained momentum as it promotes reduction in CO_2 emissions and lowers operating costs. Consequentially, EVs are becoming more popular choice over vehicles equipped with Internal Combustion Engines (ICEs). Popularity of EVs have prompted researchers to do further investigation in the functional safety of EV applications. By carrying out the Failure Mode and Effect Analysis (FMEA) for the electric drive used in an EV application, one would note that speed/position sensor failure can have catastrophic consequences, for instance on a busy roundabout or highway. Although this failure may not have a high level of exposure classification in the Automotive Safety Integrity Level (ASIL), the severity and controllability classifications are very high. Therefore it is critically important and required by the road vehicles-functional safety standards (ISO26262) for the drive mechanism, which is employed for EV applications, to be fault tolerant to the speed/position failure. The fault tolerant drive allows drivers and passengers of EVs to reach their destinations safely without disruption despite the occurrence of fault or failure [1], which is known as *limp-home* mode. Although in the *limp-home* mode the EV's drive performance may experience degradation after sustaining a fault [2], this mode increases safety, reliability and availability of the EV. The *limp-home* mode concept consists of a fault detection mechanism, a transition mechanism between sensored to sensorless control and vice versa, and more importantly, a robust and accurate speed/position estimator. In EV applications high computational effort is already required to implement various control schemes, this is to achieve the functional safety which is a critical aspect. Therefore because of the limited computational resources in the motor drive controller, the sensorless algorithm employed for fault tolerant purposes should not be too complicated.

For high performance applications, such as the EV and Hybrid EV (HEV), Torque Controlled Drives (TCDs) are usually employed for Induction Motors (IMs) [3]. From the point of view of EV applications, TCD based on field oriented control (FOC) is preferred over direct torque control (DTC). This is due to the well-known major disadvantage of DTC which is high levels of torque and current ripples [4-7]. At very low speeds, when the vehicle is pulling away, these torque distortions create an undesirable cogging effect. For EVs in which the electric motor is coupled to a gearbox, torque ripples can excite gearbox oscillations which are very hard to dampen out. Utilizing

FOC, rotor-flux angle calculation is required for transformation between stationary to synchronous reference frames and vice versa. The rotor-flux angle consists of the summation of slip and electrical rotor angles. If the speed/position signal is lost, due to sensor failure, the electrical rotor angle is estimated using a sensorless speed/position estimator scheme. In the literature, the concept of sensorless control for IM drives has been introduced for the following reasons; cost reduction, cable elimination, noise reduction, and increased reliability [8]. Assorted sensorless speed estimation techniques have been investigated in literature [9-16], including; Extended Kalman Filter (EKF) [9], Sliding Mode Observer (SMO) [10, 11], Model Reference Adaptive System (MRAS) [12, 13], Adaptive Full-order Observer (AFO) [16], and Artificial Neural Networking (ANN) based methods [14, 15]. Among the aforementioned techniques, schemes based on the MRAS are known for being simpler and requiring relatively lower computational effort [17, 18]. These MRAS schemes differ from one another by the way the error signal is calculated. These are; rotor-flux based MRAS (RF-MRAS) [19], back-electromotive force based MRAS (Back-EMF MRAS) [20, 21], reactive power based MRAS (RP-MRAS) [21], and stator current based MRAS (Is-MRAS) [22].

The RF-MRAS suffers from DC drift problems associated with pure integration and sensitivity to stator resistance variation, especially in the low speed region [13, 23, 24]. In order to improve the performance of the RF-MRAS in the low speed region, [25] had proposed second adaptation mechanism, based on electromagnetic torque, which is added to the adaptation mechanism of the RF-MRAS. Although [25] has shown that this approach improves the performance of the classical RF-MRAS at low speed, this scheme remains effected by the sensitivity to parameter variations. In [26], to improve stability of the RF-MRAS, a sliding mode stator voltage model observer is applied as the reference model. This approach introduces chattering on the torque response which is undesirable for EV applications.

The RP-MRAS scheme is immune from sensitivity to stator resistance variations, however, it has stability problems in regenerating mode [20]. The Is-MRAS, proposed in [22], shows a good performance for a wide speed range. In this scheme, the error tuning signal is calculated using the error between the measured and the estimated stator currents which then multiplied by the estimated rotor flux components. Consequently, the proposed scheme in [22], remains affected by the sensitivity to the motor parameter variations. In [27], a comparative study was carried out between modified RF-MRAS and modified back-EMF MRAS. In the modified schemes two first order low pass filter blocks have been inserted into the output and input of the reference and adjustable models, respectively. The study concluded that the adaptation gain constants of the modified RF-MRAS is easier to design.

However, the performance of the modified back-EMF MRAS is much better than the RF-MRAS at low speed region. Another comparative study in [28] also concluded that the back-EMF MRAS has better tracking capability and it fulfils the requirement as a versatile estimator. In order to make the back-EMF MRAS immune to the stator resistance variations a combined speed and stator resistance estimators were proposed in [20] to operate simultaneously. The new combined scheme is reported to improve the stability of the back-EMF MRAS and increase its robustness against the stator resistance mismatch. However, during a speed transient and no-load condition this scheme suffers from drift problems and it increases complexity compared to the conventional scheme. Although utilizing the back-EMF MRAS would eliminate challenges related to pure integration in the reference model of the RF-MRAS, sensitivity to parameters variations remains unsolved [13].

Apart from challenges related to sensitivity to parameters variations, there are other factors which may affect the performance and stability of the back-EMF MRAS scheme. For example, the inverter nonlinearity (e.g. switching dead-time and voltage drop of power semiconductor devices) causes voltage errors between the stator reference and actual input voltages of IM. At very low speed, these errors can even become larger than the motor's stator voltage [29], which can have serious effect on the performance of the back-EMF MRAS in the low speed region. Moreover, digitization effects can cause phase error in the reference model in the field weakening region [16, 30], which leads to the back-EMF MRAS instability.

In this paper, in order to deal with the aforementioned problems, a new back-EMF MRAS scheme is proposed for the purpose of fault tolerant *limp-home* mode operation in EV applications. The reference model of this scheme takes advantage of a novel compensating mechanism, to compensate for errors due to parameter variations, inverter non-linearity and digitization in high speed regions. A new approach is used in the adjustable model of this scheme which is also free from integration problems. This results in an effective sensorless control when starting from standstill and during high speed operation. Experimental testing, based on a 19 kW IM and later on an electric golf buggy (powered with 5 kW IM), are carried out to investigate the performance of the proposed scheme. A realistic speed/torque profile is used for testing purposes. Experimental results demonstrate the robustness of this scheme against motor parameter variations in addition to successful starting from standstill. The vehicle test–drive, utilizing the proposed scheme, confirms control stability and reliability during vehicle hill-starting and field weakening operation. The structure of this paper is as follows; Section II describes sensorless TCD using indirect rotor FOC (IRFOC) and a review of the fundamental concept of the conventional back-EMF MRAS scheme. Section III gives a detailed description of the proposed scheme. Section IV describes the

experimental system platform and Section V shows the experimental results of the proposed sensorless scheme. Finally the conclusion is provided in Section VI.

II. Sensorless Torque Controlled-Drive based on IRFOC using back-EMF MRAS

1. Sensorless Torque controlled-Drives based on IRFOC technique

The overall block diagram of the sensorless TCD based on IRFOC used in this paper for fault tolerant EV application is shown in Fig. 1. In EV applications the torque demand is applied by the driver using the accelerator pedal. In this approach the reference stator current on the direct-axis (i_d^*) is kept constant below base speed. Normally the sensorless speed/torque controlled drives based on the FOC techniques which have been investigated in literature [31-33], consist of an outer speed/torque control feedback loop. This is used for calculation of the reference stator current on the quadrature-axis (i_q^*) in the synchronous reference frame. Using the outer feedback loop at zero and low speeds, where almost all of the sensorless schemes struggle or fail to estimate accurately, can lead to erroneous i_q^* calculation. As far as EV applications are concerned, correct drive direction to that requested in vehicle-starting from standstill is critical. Therefore, by eliminating the outer feedback loop in sensorless TCDs a precise i_q^* calculation can be achieved, which assists the drive with vehicle-starting in the right direction from standstill.

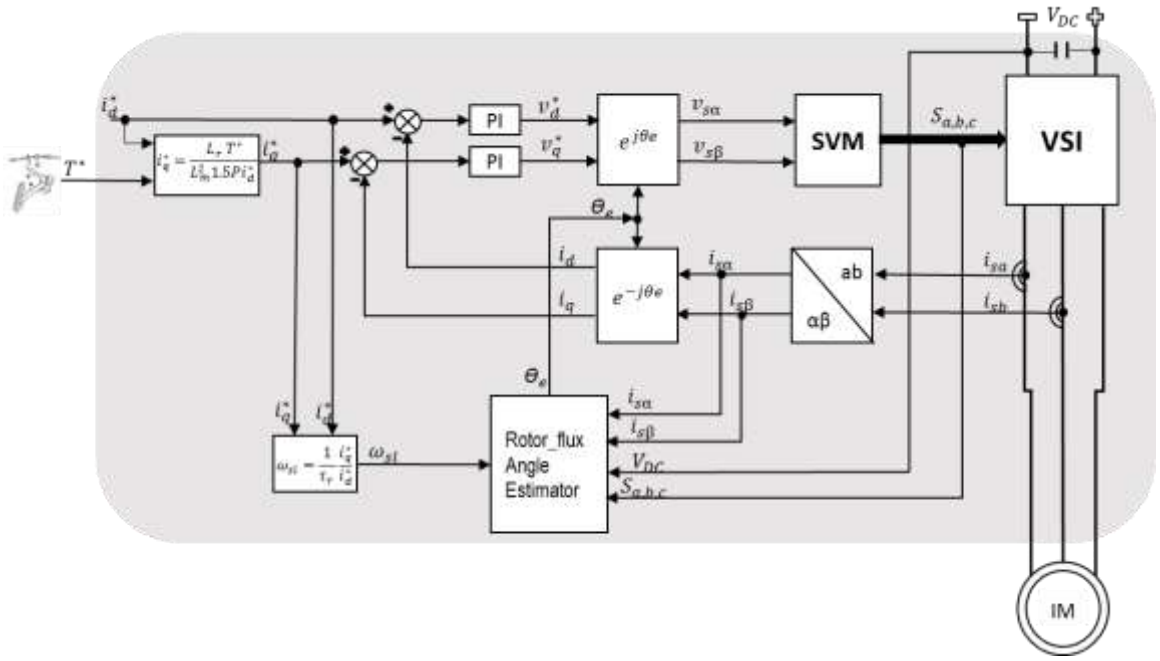

Fig. 1. Block diagram of sensorless TCD based on IRFOC.

2. Conventional back-EMF MRAS scheme

The block diagram of the conventional Back-EMF MRAS is shown in Fig. 2. For this scheme, measured stator currents and reconstructed stator voltage components in the stationary reference frame are required. The block diagram of MRAS schemes normally consist of a reference model, an adjustable model, and an adaptation mechanism. The conventional back-EMF MRAS scheme utilizes the induced back-EMF components in the stationary reference frame for the reference and adjustable models.

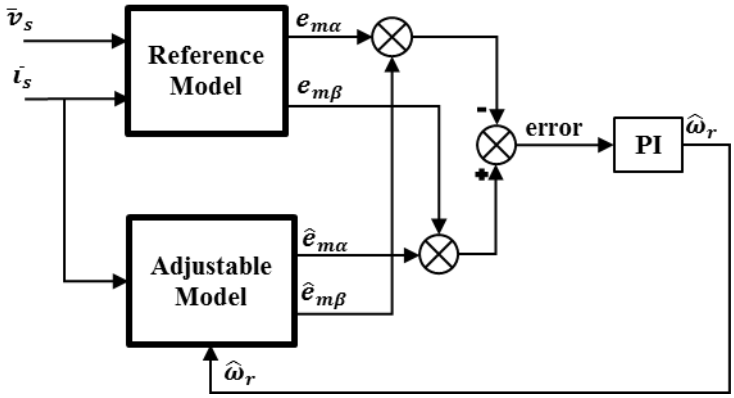

Fig. 2. Block diagram of the conventional back-EMF MRAS scheme.

The equations for the reference back-EMF components provided by the reference model can be derived from the IM stator voltage in the stationary reference frame as the following;

$$\begin{cases} v_{s\alpha} = R_s i_{s\alpha} + L_s \sigma p i_{s\alpha} + \dfrac{L_m}{L_r} p\psi_{r\alpha} \\ v_{s\beta} = R_s i_{s\beta} + L_s \sigma p i_{s\beta} + \dfrac{L_m}{L_r} p\psi_{r\beta} \end{cases} \tag{1}$$

where; $v_{s\alpha\beta}$, $i_{s\alpha\beta}$ and $\psi_{r\alpha\beta}$ are stator voltage, current and rotor flux linkage components in the stationary reference frame, respectively. R_s, L_s, L_m and L_r are stator resistance and stator self, magnetizing, and rotor inductances, respectively. $p = \frac{d}{dt}$ is the differential operator and $\sigma = 1 - (\frac{L_m^2}{L_s L_r})$ is the leakage coefficient of the machine.

In (1), $(\frac{L_m}{L_r} p\bar{\psi}_r)$ is the back-EMF term. Hence, the back-EMF of the IM in the stationary reference frame can be obtained by rearranging (1) as given below:

$$\begin{cases} e_{m\alpha} = v_{s\alpha} - R_s i_{s\alpha} - L_s \sigma p i_{s\alpha} \\ e_{m\beta} = v_{s\beta} - R_s i_{s\beta} - L_s \sigma p i_{s\beta} \end{cases} \quad (2)$$

where, ($e_{m\alpha}\ and\ e_{m\beta}$) are the reference back-EMF components in the stationary reference frame.

The equations for the estimated back-EMF components provided by the adjustable model can be written as the following;

$$\begin{cases} \hat{e}_{m\alpha} = \dfrac{L_m}{L_r}\ p\psi_{r\alpha} = \dfrac{L_m}{L_r}\dfrac{\left(L_m i_{s\alpha} - \psi_{r\alpha} - \hat{\omega}_r T_r \psi_{r\beta}\right)}{T_r} \\ \hat{e}_{m\beta} = \dfrac{L_m}{L_r}\ p\psi_{r\beta} = \dfrac{L_m}{L_r}\dfrac{(L_m i_{s\beta} - \psi_{r\beta} + \hat{\omega}_r T_r \psi_{r\alpha})}{T_r} \end{cases} \quad (3)$$

where, ($\hat{e}_{m\alpha}\ and\ \hat{e}_{m\beta}$) are the estimated back-EMF components in the stationary reference frame from the adjustable model. $T_r = \frac{L_r}{R_r}$ is the rotor time constant(where, R_r is the rotor resistance), and $\hat{\omega}_r$ is the estimated electrical rotor angular velocity.

The estimated rotor angular velocity is obtained from the adaptation mechanism.

$$\hat{\omega}_r = \left(k_p + \frac{k_i}{s}\right) * (\epsilon_\omega) \quad (4)$$

where; k_p and k_i are proportional and integral gains, respectively, and $\epsilon_\omega =$ ($\hat{e}_{m\alpha\beta} \otimes e_{m\alpha\beta}$) is the speed error tuning signal. The error tuning signal is calculated from the cross product ($\otimes$) of the estimated and the reference back-EMF components in the stationary reference frame.

III. Proposed back-EMF MRAS scheme

The block diagram of the proposed back-EMF MRAS is shown in Fig. 3. The signal flow diagrams of the reference and adjustable models of the proposed scheme are shown in Fig. 4-(a) and -(b), respectively. The reference model consists of two PI controllers which utilize errors between back-EMF components of the adjustable and reference models, to compensate for the errors due to the motor parameters variation, digitization and inverter nonlinearity. The adjustable model is based on the back-EMF in the synchronous reference frame, hence the mutual cross coupling and rotor-flux integration in (3) is no longer required. This approach promotes increase in the stability

of the MRAS schemes, due to being immune from problems related to the noise and offset accumulations caused by integration. The back-EMF components of the adjustable model are initially calculated in the synchronous reference frame and then transformed to the stationary reference frame.

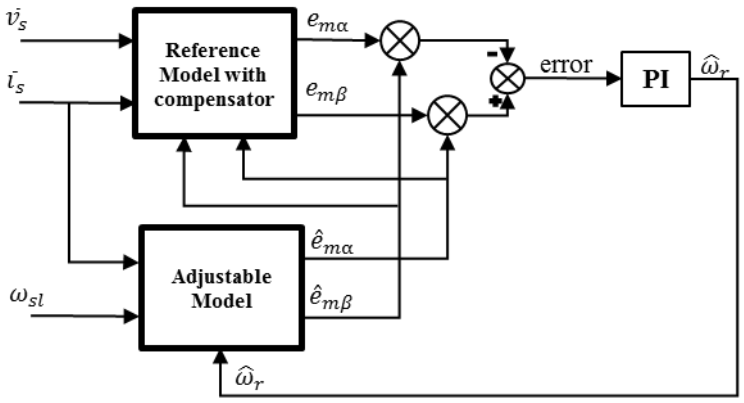

Fig. 3. Block diagram of the proposed back-EMF MRAS scheme.

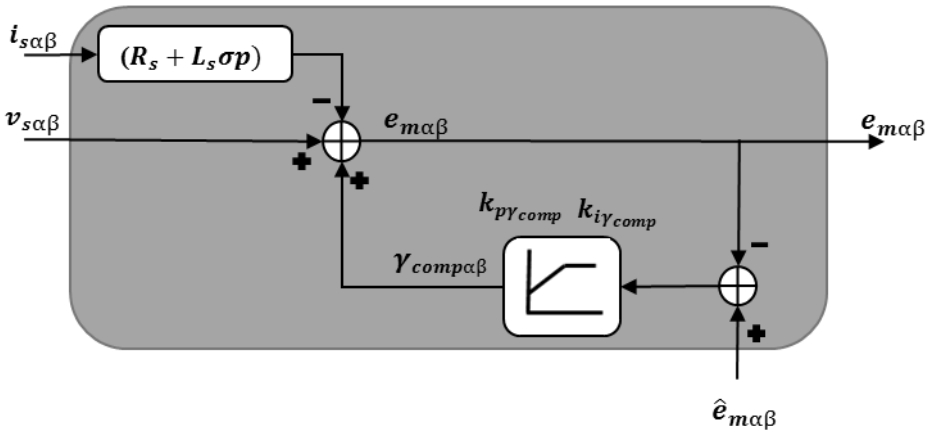

(a)

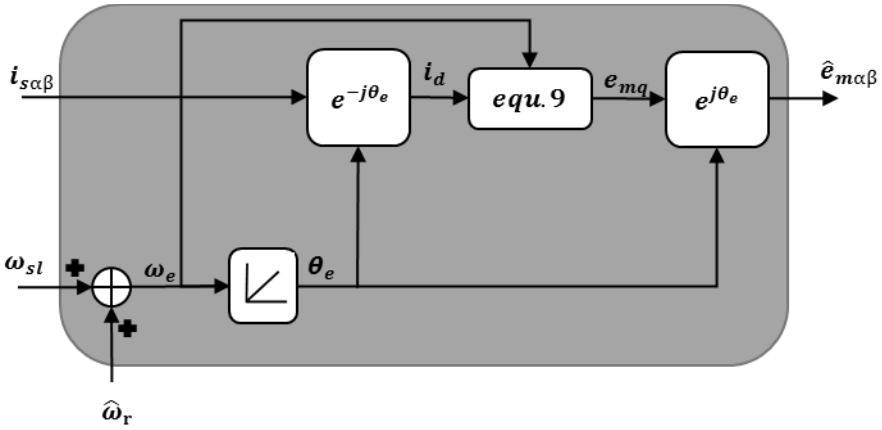

(b)

Fig. 4. Signal flow diagrams of the proposed scheme; (a) reference model and (b) adjustable model.

The back-EMF of IM can be expressed in the synchronous reference frame. This is achieved by first transferring the stator voltage equations in (1) from stationary to synchronous reference frame

$$\begin{cases} v_{sd} = (R_s + L_s\sigma p)i_{sd} + \dfrac{L_m}{L_r}p\psi_{rd} - \omega_e\left(L_s\sigma i_{sq} + \dfrac{L_m}{L_r}\psi_{rq}\right) \\ v_{sq} = (R_s + L_s\sigma p)i_{sq} + \dfrac{L_m}{L_r}p\psi_{rq} + \omega_e(L_s\sigma i_{sd} + \dfrac{L_m}{L_r}\psi_{rd}) \end{cases} \quad (5)$$

where, subscripts *d-q* represents variables in the synchronous reference frame. In the IRFOC the rotor flux is aligned with the d-axis of the synchronous reference as:

$$\psi_{rq} = 0, \qquad hence;\ \psi_r = \psi_{rd} \quad (6)$$

Where, ψ_{rd} is the d-axis rotor flux which can be obtained by

$$\psi_{rd} = L_m\, i_{sd} \quad (7)$$

Applying the IRFOC's law (6) in (5), they become

$$\begin{cases} v_{sd} = (R_s + L_s\sigma p)i_{sd} + \dfrac{L_m}{L_r}p\psi_{rd} - \omega_e L_s\sigma i_{sq} \\ v_{sq} = (R_s + L_s\sigma p)i_{sq} + \omega_e L_s\sigma i_{sd} + e_{mq} \end{cases} \quad (8)$$

where;

$$e_{mq} = \omega_e \frac{L_m}{L_r}\psi_{rd} \quad (9)$$

e_{mq} is back-EMF in the synchronous reference frame.

Note that the back-EMF term in the synchronous reference frame only appears on the q-axis. It is proportional to the rotor flux and the synchronous speed. The estimated back-EMF vector of the adjustable model is calculated by transforming (9) from the synchronous to the stationary reference frame

$$\begin{cases} \hat{e}_{m\alpha} = -\, e_{mq} * \sin(\Theta_e) \\ \hat{e}_{m\beta} = e_{mq} * \cos(\Theta_e) \end{cases} \quad (10)$$

Where, θ_e is angular position in the synchronous reference frame.

The back-EMF vector of the reference model in the stationary reference frame is calculated using the following:

$$\begin{cases} e_{m\alpha} = v_{s\alpha} - \left(R_s i_{s\alpha} + L_s \sigma \dfrac{d}{dt} i_{s\alpha}\right) + \gamma_{comp\alpha} \\ e_{m\beta} = v_{s\beta} - (R_s i_{s\beta} + L_s \sigma \dfrac{d}{dt} i_{s\beta}) + \gamma_{comp\beta} \end{cases} \tag{11}$$

Where, ($\gamma_{comp\alpha}\ and\ \gamma_{comp\beta}$) are the back-EMF compensating components. These are calculated utilizing PI controllers to drive the error between the back-EMF components of the adjustable and reference models to zero.

$$\begin{cases} \gamma_{comp_\alpha} = \left(k_{p\gamma_{comp}} + \dfrac{k_{i\gamma_{comp}}}{s}\right)\left(\epsilon_{\gamma_{comp\alpha}}\right) \\ \gamma_{comp_\beta} = \left(k_{p\gamma_{comp}} + \dfrac{k_{i\gamma_{comp}}}{s}\right)(\epsilon_{\gamma_{comp\beta}}) \end{cases} \tag{12}$$

Where; $\epsilon_{\gamma_{comp\alpha}} = \hat{e}_{m\alpha} - e_{m\alpha}$ and $\epsilon_{\gamma_{comp\beta}} = \hat{e}_{m\beta} - e_{m\beta}$ are the back-EMF error components used in the compensating mechanism.

Fig. 5 shows a block diagram of the compensating mechanism. The term $e_{m\alpha\beta_{[nom]}}$ represents the nominal back-EMF components, calculated when nominal parameters of the IM are used. The term $e_{m\alpha\beta}$ represents the output back-EMF components of the reference model. The term ΔD represents disturbances due to parameter variations ($\Delta R_s\ and\ \Delta L_s\sigma$), digitization and inverter nonlinearity which can affect the reference model. Without the compensator, the output back-EMF components include the nominal back-EMF components plus some disturbances. These disturbances can cause a steady state error, oscillation and eventually lead to instability, especially in the low speed region due to stator resistance variation and inverter nonlinearity. However, by closing the loop using the estimated back-EMF components from the adjustable model, which are free from aforementioned disturbances, the effects of ΔD can be eliminated.

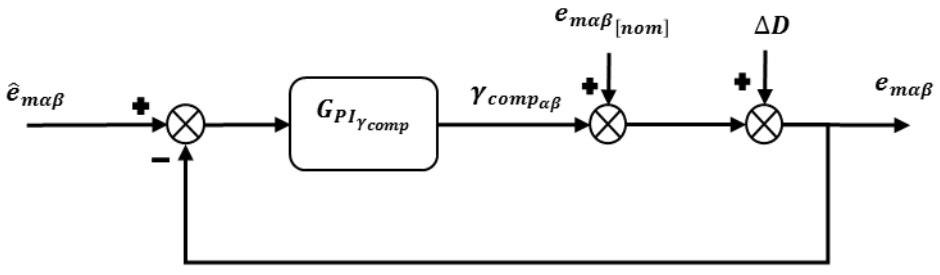

Fig. 5. Block diagram of the compensating mechanism.

The transfer function of feedback block diagram of the compensating mechanism with respect to the output back-EMF components and the control loop can be expressed by superposition of the response to the three inputs individually, as follows;

$$e_{m\alpha\beta\,cl} = \frac{G_{PI_{\gamma comp}}}{1 + G_{PI_{\gamma comp}}}\,\hat{e}_{m\alpha\beta} + \frac{1}{1 + G_{PI_{\gamma comp}}}\,e_{m\alpha\beta\,[nom]} + \frac{1}{1 + G_{PI_{\gamma comp}}}\,\Delta D \tag{13}$$

The compensating mechanism is stable if all the poles of (13) are on the left half-plane (LHP). This can be investigated in the s-plane by setting the denominator to zero, which yields;

$$\mathrm{s} = -\frac{k_{i\gamma comp}}{1 + k_{p\gamma comp}} \tag{14}$$

It can be seen that (14) is negative, hence, the compensator is stable. For the adaptation mechanism a PI controller, similar to the one used for the conventional scheme in (4), is employed to minimise error. To guarantee that the estimated rotor speed converges to the actual rotor speed, the overall proposed MRAS requires to be asymptotically stable. The overall stability of the proposed MRAS is investigated by employing a Lyapunov function V, which is expressed as below [25];

$$V = \bar{\epsilon}_{e_m}^{T}\bar{\epsilon}_{e_m} > 0 \tag{15}$$

Where, $\bar{\epsilon}_{e_m} = \begin{bmatrix} e_{m\alpha} - \hat{e}_{m\alpha} \\ e_{m\beta} - \hat{e}_{m\beta} \end{bmatrix}$ is error vector.

The state error equations can be expressed as below;

$$\dot{\bar{\epsilon}}_{e_m} = [A][\bar{\epsilon}_{e_m}] - [W] \tag{16}$$

Where;

$$A = \begin{bmatrix} -1 & 0 \\ 0 & -1 \end{bmatrix}, \qquad W = \begin{bmatrix} -\hat{e}_{s\beta} \\ \hat{e}_{s\alpha} \end{bmatrix}(\omega_r - \hat{\omega}_r) \tag{17}$$

Differentiating both side of (15), yields;

$$\dot{V} = \left(\dot{\bar{\epsilon}}_{e_m}^{T}\,\bar{\epsilon}_{e_m}\right) + \left(\bar{\epsilon}_{e_m}^{T}\,\dot{\bar{\epsilon}}_{e_m}\right) = \bar{\epsilon}_{e_m}^{T}(A^T + A)\bar{\epsilon}_{e_m} = -2\bar{\epsilon}_{e_m}^{T}\bar{\epsilon}_{e_m} \tag{18}$$

The function given in (18) is always negative. A system is said to be asymptotically stable if Lyapunov function satisfies following conditions [25, 34];

$$\begin{cases} 1)\ V = 0\ for\ \hat{\omega}_r = 0; \\ 2)\ V > 0\ for\ \left|\left|\hat{\omega}_r\right|\right| \neq 0; \\ 3)\ \dot{V} \leq 0 \end{cases} \tag{19}$$

It is clear that (15) satisfies conditions 1 and 2 of (19), this is regardless of the estimated speed direction. Moreover, (18) also satisfies condition 3 of (19). Hence, it can be state that the proposed scheme is asymptotically stable.

IV. Experimental setup

The proposed scheme was experimentally implemented and tested using a dynamometer (Dyno.) test bench which was built for the purpose of this experiment. In order to validate performance on actual EV, the scheme also was implemented and tested on an electric golf buggy. The block diagram of the overall setup, its photograph, and the golf buggy are shown in Fig. 6-(a), -(b), and -(c), respectively. The Dyno. test bench consists of a three phase 19 kW IM loaded with a surface-mounted permanent magnet synchronous motor (SPMSM). It also consists of a 300 Nm torque transducer which was used for validation. Two 29 kW generation 4 (D8-Gen4) controllers were used for driving both motors. The D8-Gen4 controllers are equipped with 32-bit floating point µ-processor, with sampling frequency of 16 kHz, and are capable of performing four quadrant control in the speed and torque modes. The stator currents were measured using two Hall sensors which are built in the controllers. In order to communicate with the D8-Gen4 on the IM, Device Verification Tool (DVT) software was utilized. During experiments the rotor speed was varied using speed throttle box connected to the D8-Gen4 which was controlling the SPMSM. The D8-Gen4 controller connected to the IM was set on the torque mode and the torque commands were applied using the laptop. The IM and SPMSM were equipped with an AB and a Sine/Cos encoders, respectively. These were used for evaluation of the implemented sensorless approach (measured speed). The sensorless control algorism was hand-coded in C-programming language and was compiled using “Keil” software development environment. The golf buggy also was equipped by a D8-Gen4 and a three phase 5 kW IM. The nominal parameters of both IMs are provided in Appendix.

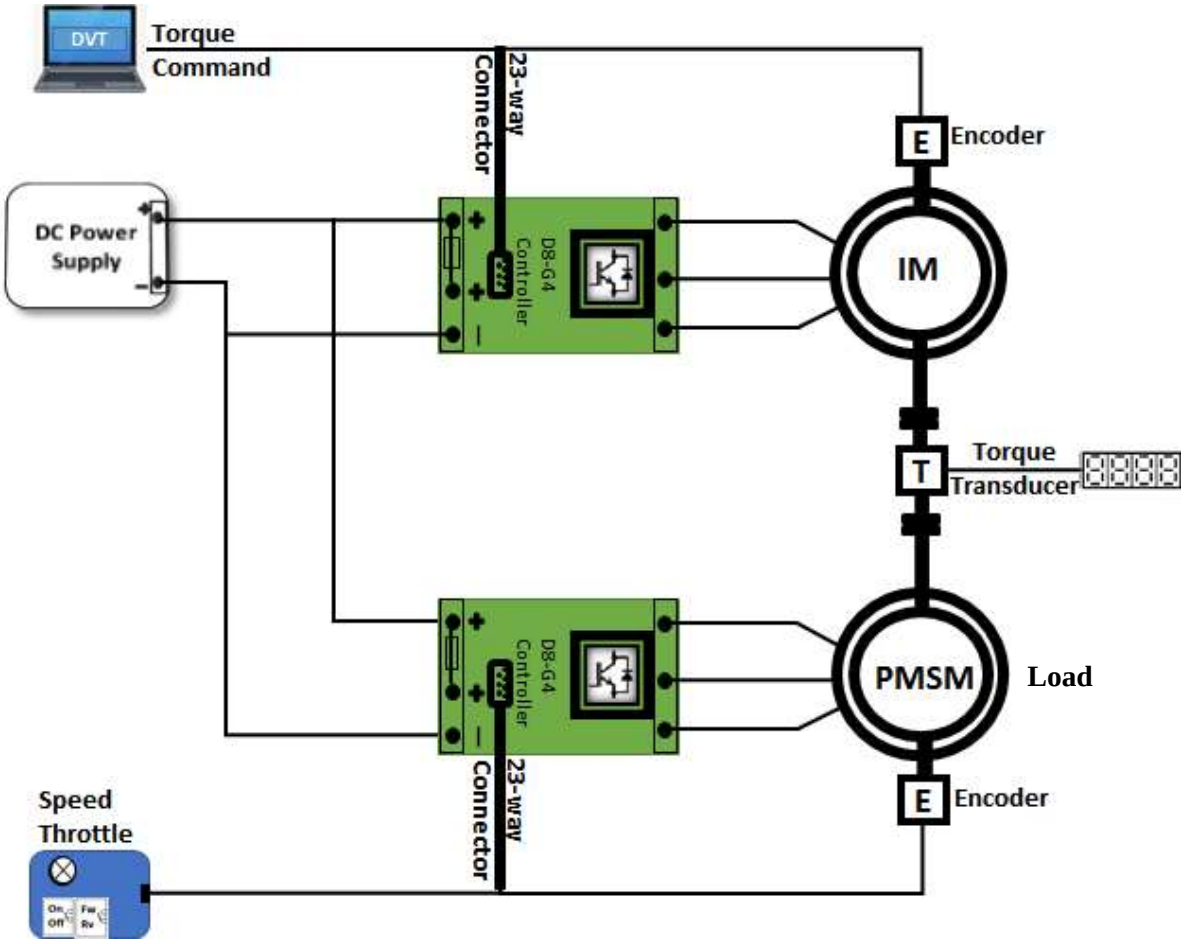
DVT
Torque
Command
23-way
Connector
E
Encoder
DC Power
Supply
D8-G4
Controller
IM
T
Torque
Transducer
PMSM
Load
Speed
Throttle
On
Off
Fw
Rv

(a)

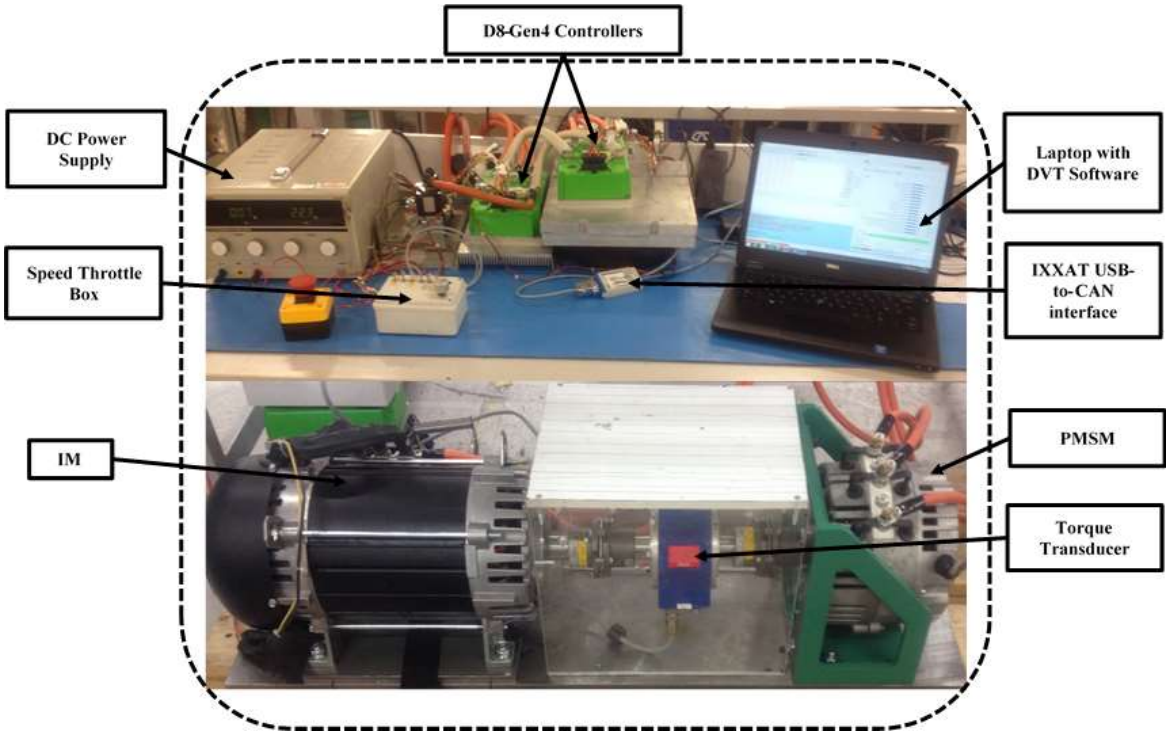
D8-Gen4 Controllers
DC Power
Supply
Laptop with
DVT Software
Speed Throttle
Box
IXXAT USB-
to-CAN
interface
IM
PMSM
Torque
Transducer

(b)

(c)

Fig. 6. Experimental setups; (a) overall block diagram, (b) actual test bench, and (c) golf buggy.

V. Experimental results and discussion

In this section, experimental results and discussion are presented to evaluate the effectiveness and feasibility of the proposed scheme for different operating conditions. Using the test bench, the performance of the proposed scheme was compared against that of the conventional back-EMF MRAS scheme. All of the experiments were conducted in the sensorless mode with the reference d-axis stator current set to a constant value ($i_d^* = 52\text{A}$). The controller has achieved software loop time 62.5 µs, bandwidth of 160 rad/s, gain margin of 25.4 db, and phase margin of 70 degree. For experiments using the golf buggy, the value of the reference d-axis stator current was produced using a Lookup Table. This was to allow the vehicle to function in the whole speed range. For these tests the measured (encoder) and estimated (sensorless) speeds were recorded.

In order to tune the estimator PI controller gains of the proposed scheme, the identical compensator PI controllers gains, were initially set to zero. To obtain the optimal dynamic performance, the adaptation PI controller gains were first tuned whilst the encoder signal was used for the transformation between reference frames. The proportional gain of the adaptation PI controller was gradually increased, while the integral gain was set to zero, until the estimator speed could approximately track the actual speed. Then the integral gain was increased to achieve faster dynamic response. After aforementioned procedure for the proposed scheme, both gains of the compensator PI controllers were set to one. This results in a small steady state error between the actual and estimated speed. By gradually decreasing both gains the error is reduced to zero. We have found that the dynamic

performance of the compensator PI controllers are more dependent on the proportional gain than the integral gain. Therefore, the integral gain can be set to any value smaller than one, as long as it is greater than zero.

Utilizing the above procedure, for experiments on the dynamometer test bench, the adaptation PI controller gains of the conventional and proposed schemes were set to ($K_p = 1\ and\ K_i = 0.1$) and ($K_p = 0.8\ and\ K_i = 0.08$), respectively. The gains of the compensator PI controllers in the reference model of the proposed scheme were set to ($k_{p\gamma_{comp}} = 0.1\ and\ k_{i\gamma_{comp}} = 0.001$). For experiments on the golf buggy, the adaptation PI controller gains of the proposed schemes were set to ($K_p = 0.9\ and\ K_i = 0.08$). The gains of the compensator PI controllers in the reference model of the proposed scheme were set to ($k_{p\gamma_{comp}} = 0.1\ and\ k_{i\gamma_{comp}} = 0.002$).

1. Experimental results from test bench

A. Starting from standstill

The sensorless IM TCD used for the purpose of fault tolerant *limp-home* mode of EV applications, must be capable of performing adequately at zero and low speeds. It is also very important to have consistency in performing vehicle-starting from standstill for consecutive attempts. Therefore this test was carried out for three consecutive attempts in forward direction to demonstrate the consistency of the conventional and the proposed back-EMF MRAS schemes for starting from standstill. During this test the speed is varied using the throttle box with the applied torque command kept at 15 Nm. Fig. 7-(a) shows the result of this test for the conventional scheme. Since, in the first attempt the conventional scheme had failed to start from standstill for an applied torque command of 15 Nm, the torque command was increased to 20 Nm and 25 Nm for the second and third attempts, respectively. From result of the proposed scheme, which is shown in Fig. 7-(b), it is clear that this scheme is consistent in starting from standstill and shows no steady-state error at zero speed.

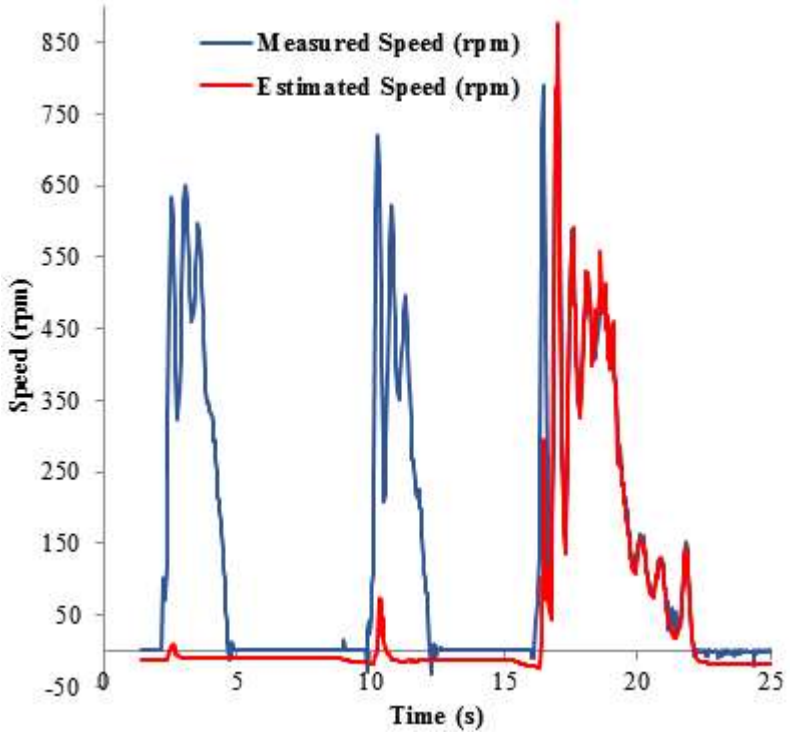

(a)

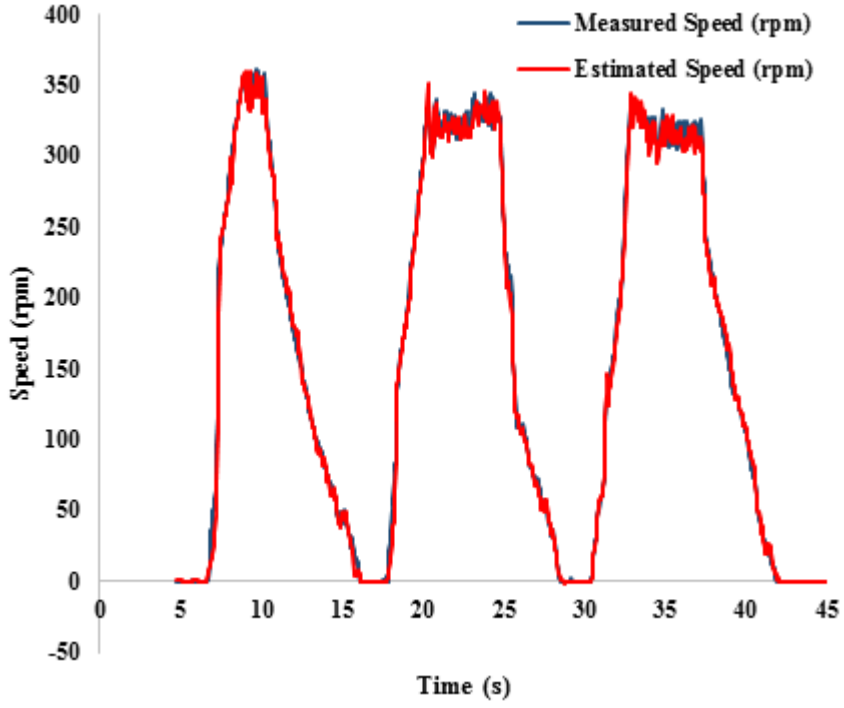

(b)

Fig. 7. Experimental results for sensorless performance starting from standstill with nominal parameters at 15 Nm. (a) Conventional Back-EMF MRAS (b) the proposed scheme.

B. Sensitivity to stator resistance variation

This test was carried out to demonstrate robustness of the proposed scheme against sensitivity to the stator resistance variations. During this test the stator resistance was increased by 50% and 100% from its nominal value and the applied torque command was kept constant at 15 Nm. Results for the conventional scheme are shown in Fig. 8-(a) and Fig. 9-(a) for cases of 50% and 100% increase in the stator resistance value, respectively. It is clear that, in the case of 50% increase, this scheme suffers from sensitivity to stator resistance variations at low speeds and it becomes more unstable for the case of 100% increase. Results of the proposed scheme are shown in Fig 8-(b) and Fig. 9-(b) for 50% and 100% increase in the stator resistance value, respectively. It is obvious that the estimated speed continuous tracking the measured speed regardless of 50% or 100% increase in the stator resistance value. Hence the proposed scheme is robust against sensitivity to the stator resistance variations.

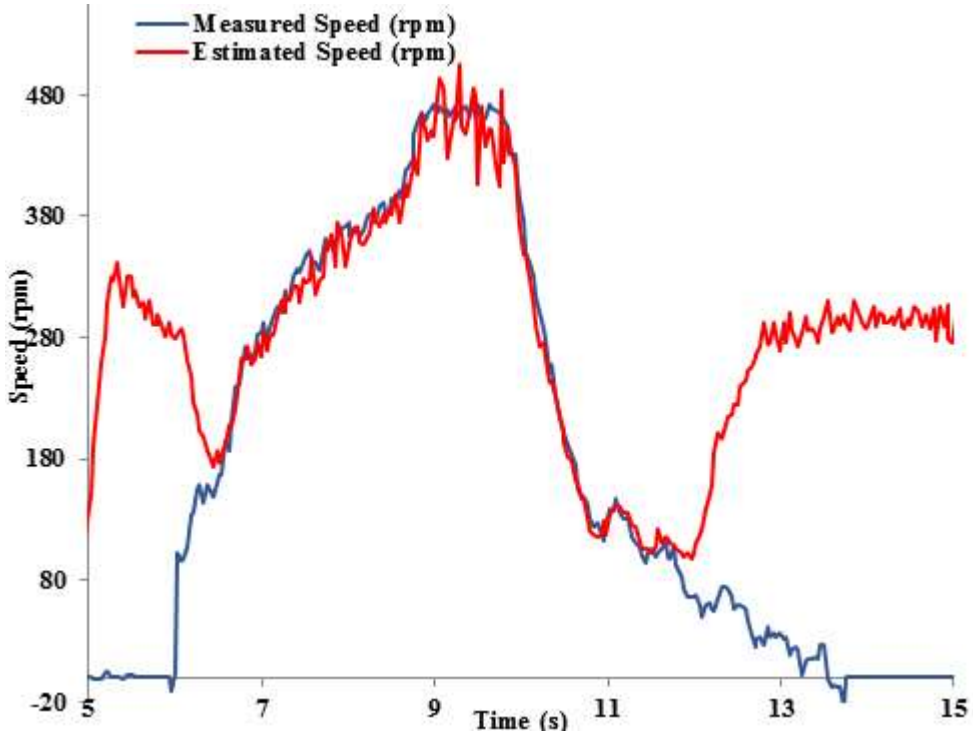

(a)

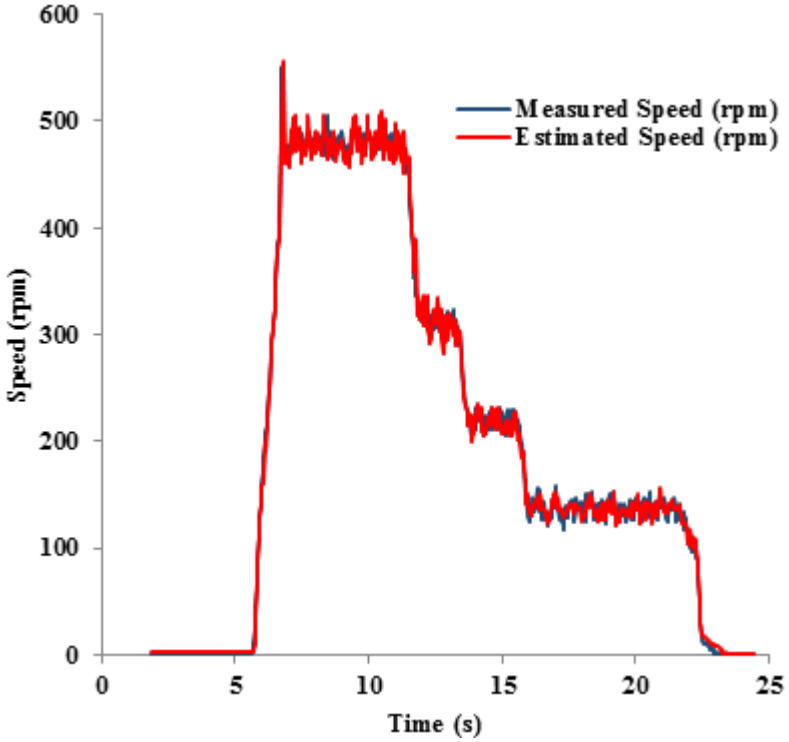

(b)

Fig. 8. Experimental results for sensorless performance with 50% increase in the stator resistance at 15 Nm. (a) Conventional Back-EMF MRAS (b) the proposed scheme.

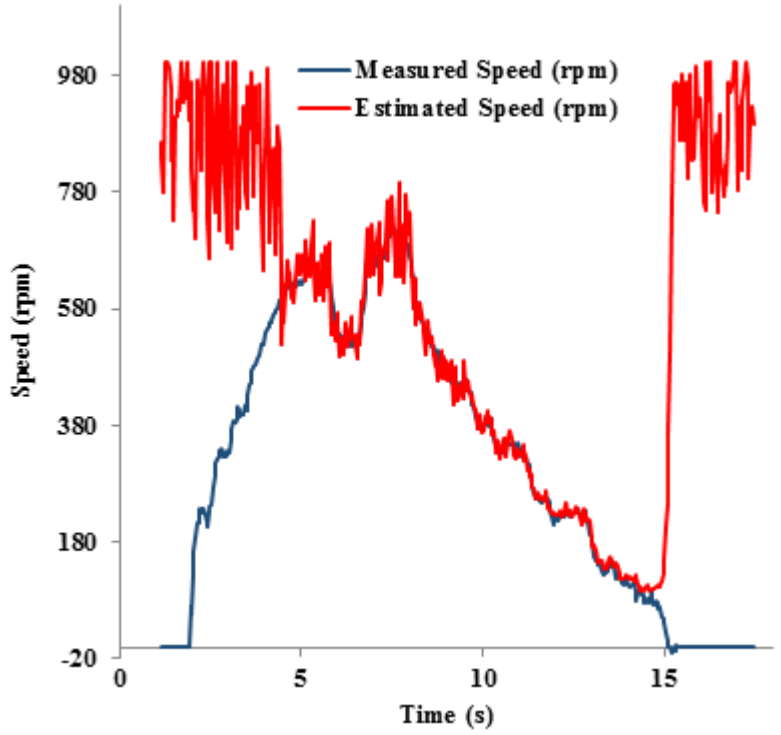

(a)

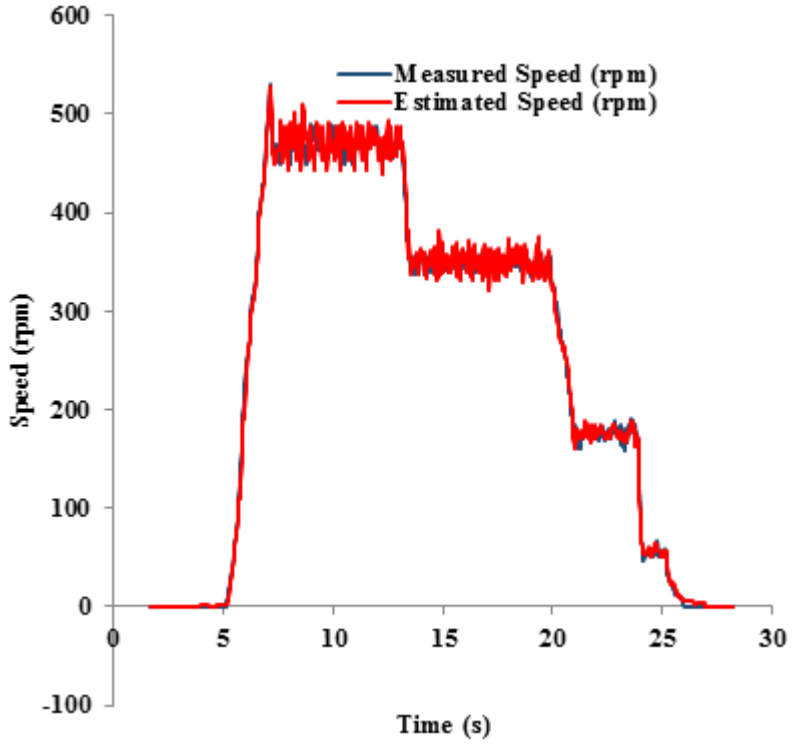

(b)

Fig. 9. Experimental results for sensorless performance with 100% increase in the stator resistance at 15 Nm. (a) Conventional Back-EMF MRAS (b) the proposed scheme.

C. Constant speed operation at different torque levels

This test was carried out to demonstrate the behaviour of the proposed scheme at constant speed with load torque variations. For this test the shaft speed was kept constant at 300 rpm with the applied torque command varied in 5 Nm intervals from 15 Nm to 50 Nm. Results of this test are shown in Fig. 10-(a) and -(b) for the conventional and proposed schemes, respectively. As can be seen, the conventional scheme has significant oscillations and at 50 Nm, it completely loses stability. Hence the estimated speed no longer tracks the measured speed. On the contrary, the proposed scheme shows much less oscillations and the estimated speed continuously tracks the measured speed closely regardless of variations in the torque command level.

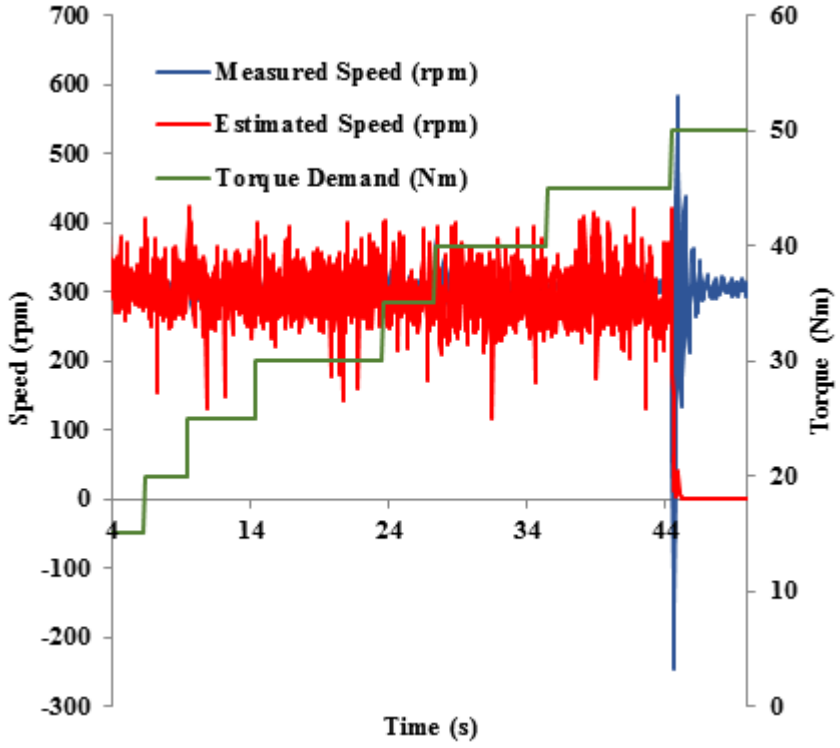

(a)

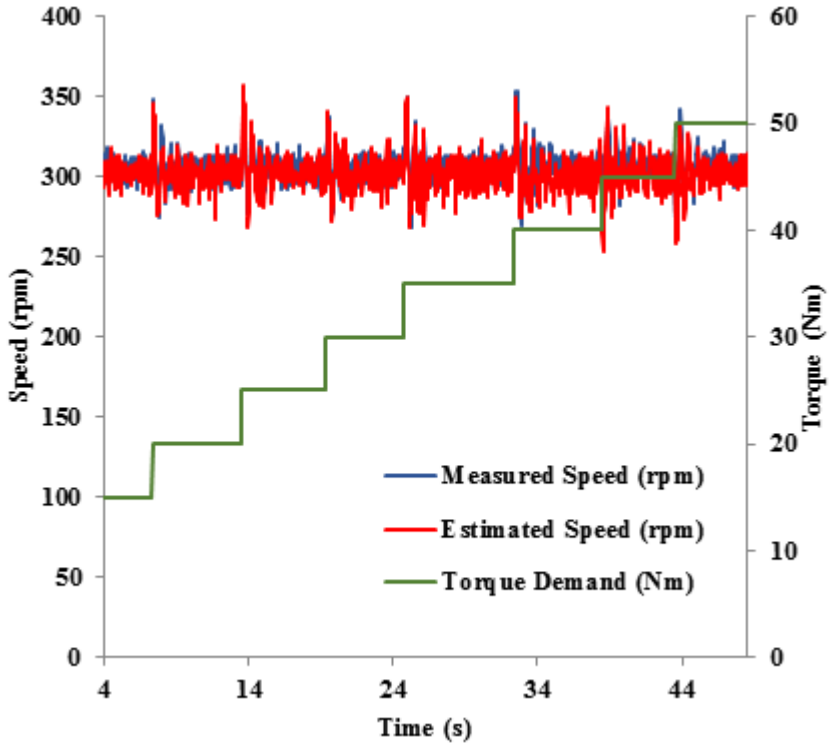

(b)

Fig. 10. Experimental results for sensorless performance at constant speed in region of 300 rpm with the torque command increased in 5 Nm intervals from 15 Nm to 50 Nm. (a) Conventional Back-EMF MRAS (b) the proposed scheme.

2. Experimental results from golf buggy

The following tests were carried out only for the proposed scheme. For these tests the estimated speed, utilizing the proposed scheme, was employed in the controller instead of the signal from the AB encoder, which was mounted on the vehicle's IM. The speed from the encoder was only used for validation which is labelled as measured speed in the recorded results. During these tests, forward, park and reverse operation modes were manually selected using the vehicle's gear stick and the torque command was applied using the accelerator pedal.

A. Vehicle test-drive for consecutive vehicle-starting from standstill

This test was carried out to confirm the capability of the proposed scheme during consecutive attempts for vehicle-starting from standstill in forward and reverse mode directions using the golf buggy. During this test, the vehicle was first driven forward and suddenly stopped by applying brake pedal, which was repeated for 5 attempts. After changing to the reverse mode the same procedure was repeated for the reverse direction for 3 attempts. The result

of this test is shown in Fig. 11. It is clear that the estimated speed tracks the measured speed very closely in both directions and despite sudden changes in the vehicle speed the estimator remains stable and consistent in vehicle-starting from standstill.

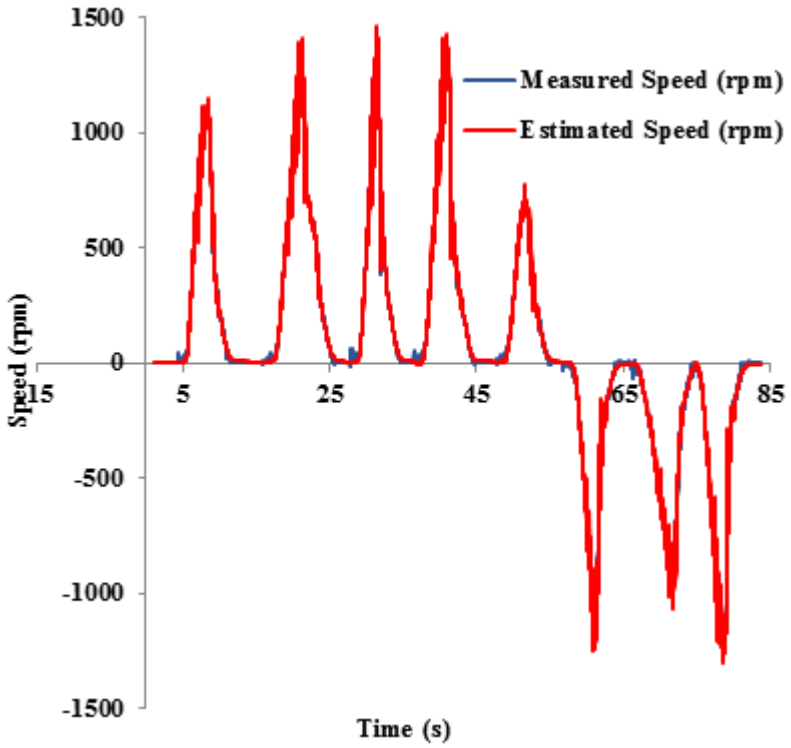

Fig. 11. Experimental result from Golf buggy. Sensorless vehicle-starting from standstill for consecutive attempts in forward and reverse modes of operation.

B. Forward and reverse test-drive in wide speed range

It is required that sensorless schemes used for EV applications be capable of performing in a wide speed range, especially in the field weakening region. Therefore this test was carried out to demonstrate the capability of the proposed scheme for wide range of speeds. During this test the vehicle was accelerated forward to around +2860 rpm and then slowed down to zero and the same procedure was repeated in the reverse direction for the speed around -2860 rpm. Fig. 12 shows the result of this test, which confirms the capability and reliability of the proposed scheme across the whole speed range. Moreover, utilising the proposed scheme provides a smooth test-drive in wide speed range. Note that deeper field weakening was prevented due to limited length of the test-track but we have found that, with the static testing, further field weakening approximately twice the base speed can easily be achieved.

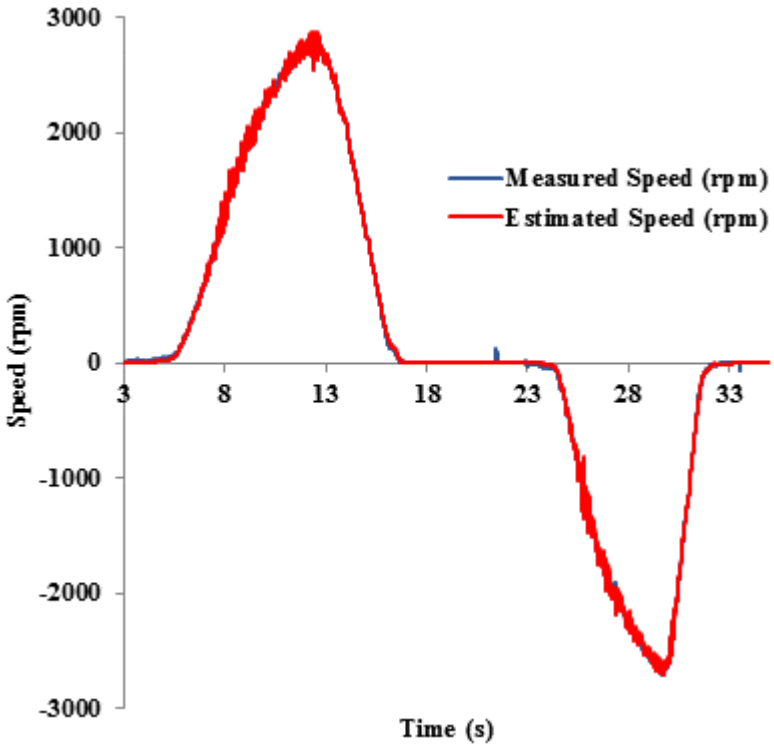

Fig. 12. Experimental result from Golf buggy. Sensorless vehicle test-drive in wide speed range for forward and reverse modes drive operation.

C. Vehicle hill-starting performance

This test was carried out to demonstrate the behaviour of the proposed scheme during vehicle hill-starting. In order to create a realistic worst case scenario, this test was carried out after 30 mins of the vehicle test-drive to increase the motor's temperature, hence increase in the stator resistance above its nominal value. A 15 degree ramp, which is especially designed for the vehicle hill-starting test, was used for purpose of this test. In order to prevent the vehicle from rolling backwards, a torque command of around 5 Nm was initially applied, using the accelerator pedal. The torque command was gradually increased to cause the vehicle to move forward and then the accelerator was gradually eased back to reduce the torque command to around 5 Nm again. The result of this test is shown in Fig. 13, which illustrates stability and reliability of this scheme during the vehicle hill-starting. It is clear that the vehicle did not roll backward during standstill period while it was on the ramp.

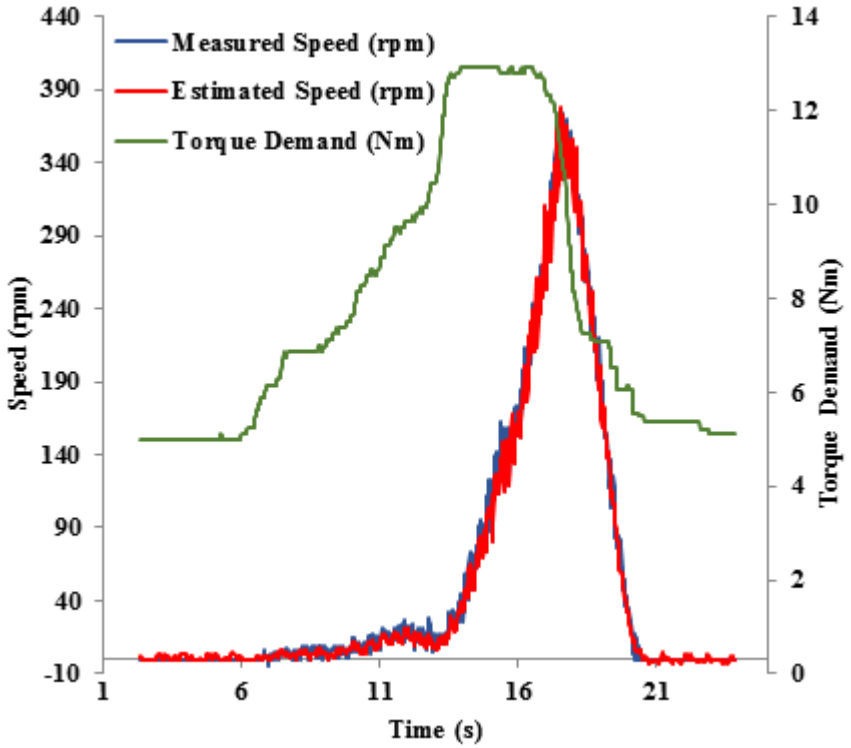

Fig. 13. Experimental result from Golf buggy. Sensorless vehicle test-drive in hill-starting for forward mode drive operation.

VI. Conclusion

A novel back-EMF MRAS speed estimator is described in this paper for the purpose of sensorless TCD employed for the fault tolerant limp-home mode EV applications. The proposed scheme was successfully implemented and tested on two different IMs using a laboratory test bench and an EV (a golf buggy), respectively. This scheme is not computationally demanding and is robust against stator resistance variations of 50% and 100% increase. The proposed scheme is not only consistent and stable for the vehicle-starting from standstill and low speeds, it also performs reliably above base speed in the field weakening region. During the tests, the proposed scheme had shown satisfactory operation throughout forward and backword modes of operation in addition to the constant speed variable load operation. More importantly the scheme had demonstrated satisfactory performance for vehicle hill-starting. Therefore the proposed back-EMF MRAS scheme is suitable for the limp-home mode operation of EV applications by providing consistent, safe and reliable operation over the whole speed range.

Appendix

TABLE I. NOMINAL PARAMETERS OF IM USED IN EXPERIMENTAL SETUP

Power [kW]	**19**	**Stator inductance [H]**	$2.9811 * 10^{-4}$
DC link voltage [V]	**65**	**Rotor inductance [H]**	$2.9810 * 10^{-4}$
Phase voltage [V] (rms)	**27**	**Stator resistance [Ω]**	$3.6 * 10^{-3}$
Rated torque [N.m]	**100**	**Rotor resistance [Ω]**	$3.1 * 10^{-3}$
Rated frequency [Hz]	**52**	**Magnetizing inductance [H]**	$8.85 * 10^{-4}$
Rated current [A] (rms)	**450**	**Number of Pole pairs**	**2**

TABLE II. NOMINAL PARAMETERS OF 5 kW IM FOR ELECTRIC GOLF BUGGY

Power [kW]	**5**	**Stator inductance [H]**	$85.027 * 10^{-4}$
DC link voltage [V]	**48**	**Rotor inductance [H]**	$37.344 * 10^{-4}$
Phase voltage [V] (rms)	**28**	**Magnetizing inductance [H]**	$7.78 * 10^{-4}$
Rated torque [N.m]	**21**	**Rotor resistance [Ω]**	$4.45 * 10^{-3}$
Rated frequency [Hz]	**78**	**Stator resistance [Ω]**	$10.24 * 10^{-3}$
Rated current [A] (rms)	**138**	**Number of Pole pairs**	**2**

Reference

[1] M. E. H. Benbouzid, D. Diallo, and M. Zeraoulia, “Advanced Fault-Tolerant Control of Induction-Motor Drives for EV/HEV Traction Applications: From Conventional to Modern and Intelligent Control Techniques,” *IEEE Trans. Veh. Technol.,* vol. 56, no. 2, pp. 519-528, 2007.

[2] D. Diallo, M. E. H. Benbouzid, and A. Makouf, “A fault-tolerant control architecture for induction motor drives in automotive applications,” *IEEE Trans. Veh. Technol.,* vol. 53, no. 6, pp. 1847-1855, 2004.

[3] D. O. Neacsu, and K. Rajashekara, “Comparative analysis of torque-controlled IM drives with applications in electric and hybrid vehicles,” *IEEE Trans. Power Electron.,* vol. 16, no. 2, pp. 240-247, 2001.

[4] I. M. Alsofyani, and N. R. N. Idris, “Simple Flux Regulation for Improving State Estimation at Very Low and Zero Speed of a Speed Sensorless Direct Torque Control of an Induction Motor,” *IEEE Trans. Power Electron.,* vol. 31, no. 4, pp. 3027-3035, 2016.

[5] D. Casadei, F. Profumo, G. Serra, and A. Tani, “FOC and DTC: two viable schemes for induction motors torque control,” *IEEE Trans. Power Electron.,* vol. 17, no. 5, pp. 779-787, 2002.

[6] V. S. S. P. K. Hari, and G. Narayanan, “Theoretical and Experimental Evaluation of Pulsating Torque Produced by Induction Motor Drives Controlled with Advanced Bus-Clamping Pulse Width Modulation,” *IEEE Trans. Ind. Electron.,* vol. PP, no. 99, pp. 1-1, 2015.

[7] K. B. Lee, and F. Blaabjerg, “Sensorless DTC-SVM for Induction Motor Driven by a Matrix Converter Using a Parameter Estimation Strategy,” *IEEE Trans. Ind. Electron.,* vol. 55, no. 2, pp. 512-521, 2008.

[8] J. Holtz, “Sensorless control of induction motor drives,” *Proceedings of the IEEE,* vol. 90, no. 8, pp. 1359-1394, 2002.
[9] Y. Zhong-gang, Z. Chang, Z. Yan-ru, and L. Jing, “Research on Robust Performance of Speed-Sensorless Vector Control for the Induction Motor Using an Interfacing Multiple-Model Extended Kalman Filter,” *IEEE Trans. Power Electron.,* vol. 29, no. 6, pp. 3011-3019, 2014.
[10] S. A. Davari, D. A. Khaburi, F. Wang, and R. M. Kennel, “Using Full Order and Reduced Order Observers for Robust Sensorless Predictive Torque Control of Induction Motors,” *IEEE Trans. Power Electron.,* vol. 27, no. 7, pp. 3424-3433, 2012.
[11] S. Di Gennaro, J. Rivera Dominguez, and M. A. Meza, “Sensorless High Order Sliding Mode Control of Induction Motors With Core Loss,” *IEEE Trans. Ind. Electron.,* vol. 61, no. 6, pp. 2678-2689, 2014.
[12] A. K. Abdelsalam, M. I. Masoud, M. S. Hamad, and B. W. Williams, “Improved Sensorless Operation of a CSI-Based Induction Motor Drive: Long Feeder Case,” *IEEE Trans. Power Electron.,* vol. 28, no. 8, pp. 4001-4012, 2013.
[13] A. V. Ravi Teja, V. Verma, and C. Chakraborty, “A New Formulation of Reactive-Power-Based Model Reference Adaptive System for Sensorless Induction Motor Drive,” *IEEE Trans. Ind. Electron.,* vol. 62, no. 11, pp. 6797-6808, 2015.
[14] M. Cirrincione, A. Accetta, M. Pucci, and G. Vitale, “MRAS Speed Observer for High-Performance Linear Induction Motor Drives Based on Linear Neural Networks,” *IEEE Trans. Power Electron.,* vol. 28, no. 1, pp. 123-134, 2013.
[15] S. M. Gadoue, D. Giaouris, and J. W. Finch, “Sensorless Control of Induction Motor Drives at Very Low and Zero Speeds Using Neural Network Flux Observers,” *IEEE Trans. Ind. Electron.,* vol. 56, no. 8, pp. 3029-3039, 2009.
[16] B. Wang, Y. Zhao, Y. Yu, G. Wang, D. Xu, and Z. Dong, “Speed-Sensorless Induction Machine Control in the Field-Weakening Region Using Discrete Speed-Adaptive Full-Order Observer,” *IEEE Trans. Power Electron.,* vol. 31, no. 8, pp. 5759-5773, 2016.
[17] S. M. Gadoue, D. Giaouris, and J. W. Finch, “MRAS Sensorless Vector Control of an Induction Motor Using New Sliding-Mode and Fuzzy-Logic Adaptation Mechanisms,” *IEEE Trans. Energy Convers.,* vol. 25, no. 2, pp. 394-402, 2010.
[18] J. W. Finch, and D. Giaouris, “Controlled AC Electrical Drives,” *IEEE Trans. Ind. Electron.,* vol. 55, no. 2, pp. 481-491, 2008.
[19] C. Schauder, “Adaptive speed identification for vector control of induction motors without rotational transducers,” *IEEE Trans. Ind. Appl.,* vol. 28, no. 5, pp. 1054-1061, 1992.
[20] M. Rashed, and A. F. Stronach, “A stable back-EMF MRAS-based sensorless low-speed induction motor drive insensitive to stator resistance variation,” *IEE Proceedings -Electric Power Applications,* vol. 151, no. 6, pp. 685-693, 2004.
[21] F. Z. Peng, and T. Fukao, “Robust speed identification for speed-sensorless vector control of induction motors,” *IEEE Trans. Ind. Appl.,* vol. 30, no. 5, pp. 1234-1240, 1994.
[22] T. Orlowska-Kowalska, and M. Dybkowski, “Stator-Current-Based MRAS Estimator for a Wide Range Speed-Sensorless Induction-Motor Drive,” *IEEE Trans. Ind. Electron.,* vol. 57, no. 4, pp. 1296-1308, 2010.
[23] Y. B. Zbede, S. M. Gadoue, and D. J. Atkinson, “Model Predictive MRAS Estimator for Sensorless Induction Motor Drives,” *IEEE Trans. Ind. Electron.,* vol. PP, no. 99, pp. 1-1, 2016.
[24] A. N. Smith, S. M. Gadoue, and J. W. Finch, “Improved Rotor Flux Estimation at Low Speeds for Torque MRAS-Based Sensorless Induction Motor Drives,” *IEEE Trans. Energy Convers.,* vol. 31, no. 1, pp. 270-282, 2016.
[25] I. Benlaloui, S. Drid, L. Chrifi-Alaoui, and M. Ouriagli, “Implementation of a New MRAS Speed Sensorless Vector Control of Induction Machine,” *IEEE Trans. Energy Convers.,* vol. 30, no. 2, pp. 588-595, 2015.

[26] F. Wang, S. A. Davari, Z. Chen, Z. Zhang, D. A. Khaburi, J. Rodriguez, and R. Kennel, “Finite Control Set Model Predictive Torque Control of Induction Machine with a Robust Adaptive Observer,” *IEEE Trans. Ind. Electron.,* vol. PP, no. 99, pp. 1-1, 2016.

[27] M. N. Marwali, and A. Keyhani, "A comparative study of rotor flux based MRAS and back EMF based MRAS speed estimators for speed sensorless vector control of induction machines." pp. 160-166 vol.1.

[28] A. R. Haron, and N. R. N. Idris, "Simulation of MRAS-based Speed Sensorless Estimation of Induction Motor Drives using MATLAB/SIMULINK." pp. 411-415.

[29] G. Shen, W. Yao, B. Chen, K. Wang, K. Lee, and Z. Lu, “Automeasurement of the Inverter Output Voltage Delay Curve to Compensate for Inverter Nonlinearity in Sensorless Motor Drives,” *IEEE Trans. Power Electron.,* vol. 29, no. 10, pp. 5542-5553, 2014.

[30] D. P. Mar, x010D, eti, x, I. R. Kr, x010D, mar, M. A. Geci, x, P. R. Mati, and x, “Discrete Rotor Flux and Speed Estimators for High-Speed Shaft-Sensorless IM Drives,” *IEEE Trans. Ind. Electron.,* vol. 61, no. 6, pp. 3099-3108, 2014.

[31] M. F. Iacchetti, G. D. Marques, and R. Perini, “Torque Ripple Reduction in a DFIG-DC System by Resonant Current Controllers,” *IEEE Trans. Power Electron.,* vol. 30, no. 8, pp. 4244-4254, 2015.

[32] L. Zhao, J. Huang, J. Chen, and M. Ye, “A Parallel Speed and Rotor Time Constant Identification Scheme for Indirect Field Oriented Induction Motor Drives,” *IEEE Trans. Power Electron.,* vol. PP, no. 99, pp. 1-1, 2015.

[33] D. Stoji, x, M. Milinkovi, x, S. Veinovi, x, I. Klasni, and x, “Improved Stator Flux Estimator for Speed Sensorless Induction Motor Drives,” *IEEE Trans. Power Electron.,* vol. 30, no. 4, pp. 2363-2371, 2015.

[34] G. F. Franklin, J. D. Powell, and A. Emami-Naeini, *Feedback Control of Dynamic Systems*, 6th ed., p.^pp. 654-660, Upper Saddle River: Pearson Education, 2010.